ELSEVIER

Available online at www.sciencedirect.com

ScienceDirect

Focus Article, *Mendeleev Commun.*, 2022, **32**, 152–163

Mendeleev
Communications

# Superhard boron suboxide ($B_6O$): crystal structure, synthesis, properties, applications, and materials based thereon

**Sergey N. Perevislov**

*I. V. Grebenshchikov Institute of Silicate Chemistry, Russian Academy of Sciences,*
*199034 St. Petersburg, Russian Federation. E-mail: perevislov@mail.ru*

DOI: 10.1016/j.mencom.2022.03.002

**A review of reported data on the crystal structure, synthesis, and properties of boron suboxide $B_6O$, which is a superhard material (hardness of up to 55 GPa, as measured in single crystals), and composites based on it is presented. Methods for the synthesis of $B_6O$ with a icosahedral structure and for the growing of crystals at high temperature and high pressure are described. The mechanical and operational characteristics of composite materials based on $B_6O$ are summarized; the resistance of $B_6O$ to oxidation is analyzed, and the properties of $B_6O$–diamond and $B_6O$–$B_4C$ composite materials are described.**

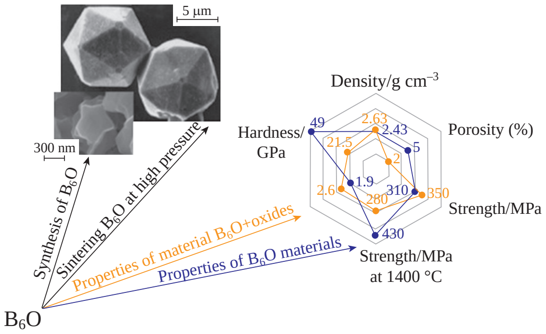

*Keywords*: boron suboxide, $B_6O$ synthesis, $B_6O$ materials, superhard material, mechanical properties, $B_6O$–diamond and $B_6O$–$B_4C$ composites.

## 1. Introduction

Boron is one of the most interesting elements of the periodic table. It exists in 16 allotropic forms stabilized by various impurities. The well-known undoped allotropic forms of boron, *viz*., α, β, γ and tetragonal t-form, are superhard.[1] In 2016,[2] two more boron modifications were discovered, namely, τ-B and borofen, a two-dimensional (2D) allotropic boron modification.[3,4] Boron oxide $B_2O_3$ and boron suboxide $B_6O$ are well known and described in the literature.[4–15]

Two crystalline forms of boron oxide, which occur at atmospheric pressure ($B_2O_3^{I}$)[5] and at high pressure ($B_2O_3^{II}$),[6] are known to date. $B_2O_3^{I}$ is built of triangular $BO_3$ blocks, while $B_2O_3^{II}$ consists of $BO_4$ tetrahedra. The boron oxide transformations $B_2O_3 \rightarrow BO_3 \rightarrow BO_4 \rightarrow BO_5 \rightarrow BO_6$ under high pressure were reported.[8,9]

The boron suboxides $B_2O$,[11] $B_6O$,[12] $B_{13}O_2$,[13] $B_7O$,[14] and $B_{22}O$[15] (with the exception of $B_2O$) are promising superhard materials. The suboxides $B_6O$, $B_{13}O_2$, $B_7O$, and $B_{22}O$ are characterized by a rhombohedral α-B structure with icosahedral $B_{12}$ units bound by oxygen atoms. Among boron suboxides, $B_6O$ has been studied most thoroughly. The small interatomic bond length and highly covalent nature[11,16–19] determine $B_6O$ properties such as high hardness, low density, high thermal conductivity, good chemical inertness, and excellent wear resistance. Figure 1 shows a histogram of the microhardnesses of various superhard

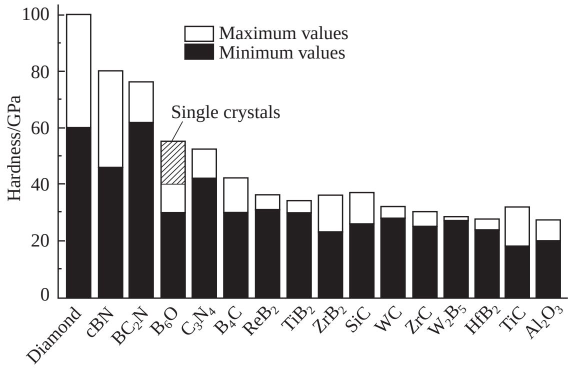

**Figure 1** Histogram of the microhardnesses of various superhard materials. Reproduced with permission from ref. 20. © 2013 Elsevier.

**Sergey N. Perevislov** was born in Russia (Leningrad, currently St. Petersburg). Doctor of Technical Sciences (2018). The degree was defended at the A. A. Baikov Institute of Metallurgy and Materials Science of the Russian Academy of Sciences. S. N. Perevislov performed his work at the Department of Technology of Refractory Nonmetallic and Silicate Materials of the St. Petersburg State Technological Institute (Technical University). Currently he is employed as senior researcher at I. V. Grebenshchikov Institute of Silicate Chemistry of the Russian Academy of Sciences. Main research interests: materials science, ceramics, silicate materials, physical chemistry, oxygen-free compounds, high-hardness, high-strength materials and composites. He is an author of over 100 scientific articles, 10 Russian Federation patents, and reports at more than 70 conferences.

materials.[20] The highest hardness (except for diamond) is manifested by materials that consist of light elements and are rich in boron. The majority of these compounds (cBN, $BC_2N$, $B_6O$, $B_4C$, and $ReB_2$) have unique crystal structures and interesting physicochemical properties.[11,17] Materials based on $B_6O$ are among the hardest ones: $HV = 45–55$ GPa (in single crystals).[17–19] $B_6O$ is synthesized under atmospheric pressure,[21] in contrast to diamond[22] and cubic cBN[23] synthesized at high pressures.

This paper presents a literature review on the superhard boron suboxide $B_6O$. The crystal structure of $B_6O$ and methods for its synthesis are considered along with studies on the morphology and properties of powder materials and composites synthesized on the basis of $B_6O$.

## 2. Crystal structure and properties of $B_6O$

The crystal structure of $B_6O$ consists of cubic α-B structures that form icosahedral $B_{12}$ units.[20,24–27] Oxygen atoms are located between icosahedral structures, slightly reducing the *c*/*a* ratio in comparison with the structure of α-B. The crystal structure of $B_6O$ resembles that of boron carbide (Figure 2).[28] Boron carbide has a wide range of compositions due to incomplete population of oxygen positions between the $B_{12}$ blocks in the structure of $B_4C$. Therefore, it is extremely difficult to obtain stoichiometric $B_6O$ in a synthesis under atmospheric pressure. A synthesis at a low pressure and high temperature gives the oxygen-depleted compound $B_6O_{1-x}$, where $x \leqslant 0.28$.[24,29–33] Boron suboxide $B_7O$ corresponds to the formula $B_6O_{0.86}$, which is within the homogeneity range of $B_6O$.

Boron suboxide exists in two space groups, *R*3*m*-$B_6O$[21] and *Cmcm*-$B_6O$. The enthalpy difference between $B_6O$ forms with different space groups is small (at atmospheric pressure, it is only 1.8 meV per formula unit, and it slightly increases with pressure).[34] The crystal lattice parameters of the hexagonal unit cell of stoichiometric *R*3*m*-$B_6O$ (80.24 at% B) are $a = 5.328$ and $c = 12.344$ Å, as calculated by means of interpolation.[35]

According to Bolmgren *et al.*,[25] oxygen atoms are located near the center of boron triangles of three $B_{12}$ icosahedra marked as B(1) and B(2) atoms in Figure 3. A large interatomic distance between the oxygen atoms (3.062 Å) indicates that they nearly do not interact. Figure 4 shows a diagram of the arrangement of B(1), B(2), and O atoms in *R*3*m*-$B_6O$, and Table 1 summarizes the interatomic distances of the B(1), B(2), and O atoms.[25]

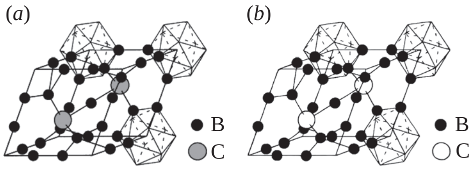

**Figure 2** Crystal structures of (*a*) $B_4C$ and (*b*) $B_6O$. Reproduced with permission from ref. 28. © 2002 Japan Institute of Metals.

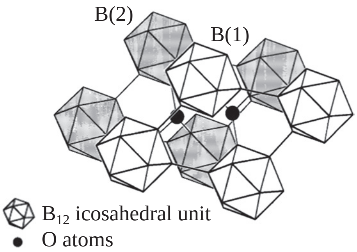

**Figure 3** *R*3*m*-$B_6O$ space group consisting of eight icosahedra and two oxygen atoms that form a rhombohedral unit cell. Gray icosahedra $B_{12}$ in the background consist of B(1) atoms. Reproduced with permission from ref. 26. © 1998 American Chemical Society.

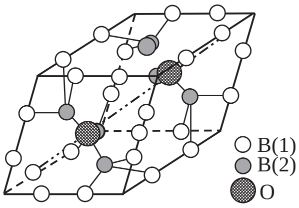

**Figure 4** Arrangement of B(1), B(2) and O atoms in *R*3*m*-$B_6O$. B(1) and B(2) indicate the atoms that form gray and white $B_{12}$ icosahedra, respectively. Reproduced with permission from ref. 25. © 1991 American Institute of Physics.

**Table 1** Interatomic distances in the *R*3*m*-$B_6O$ structure.[25]

| Atomic bond | Interatomic distance/Å |
|---|---|
| B(1)–O | 1.5037 |
| B(1)–B(1) | 1.7389 |
| B(1)–B(2) | 1.8410 |
| B(2)–B(2) | 1.5620 |
| O–O | 3.0700 |

According to Bills *et al.*,[35] the lattice parameters of nonstoichiometric $B_6O$ vary depending on the excess or deficiency of oxygen: some intermediate oxygen atoms in samples with oxygen deficiency (80.5 and 81.0 at% B) are missing and replaced by boron atoms to form a $B_{12}(O_{2-x}B_x)$ structural unit. Since a boron atom is smaller than the oxygen atom it replaces, this results in an increase in the parameter *a* and a decrease in the parameter *c* (Figure 5). It is expected that the presence of vacancies instead of oxygen atoms would lead to the opposite effect, that is, a decrease in *a* and an increase in *c*. In oxygen-rich samples (79.7, 79.9, and 80.1 at% B), it is likely that intermediate oxygen is incorporated to give the $B_{12}O_{2+x}$ structural unit, which results in an increase in *a* and a decrease in *c*. If oxygen in the $B_{12}O_2$ structural unit is simply replaced by a boron atom in the large boron icosahedron, it does almost not affect the parameters *a* and *c*.

Of all boron oxides, only $B_2O_3$ and $B_6O$ are stable compounds.[36,37] Moreover, $B_6O$ is stable only at pressures below 94 GPa, while $B_2O_3$ remains the only stable boron oxide at higher pressures.

In 2016, the *Cmcm*-$B_6O$ space group was predicted[12] and then confirmed experimentally[38] (Figure 6); the stable $B_6O$ phase has this group in a range from atmospheric pressure to 94 GPa.

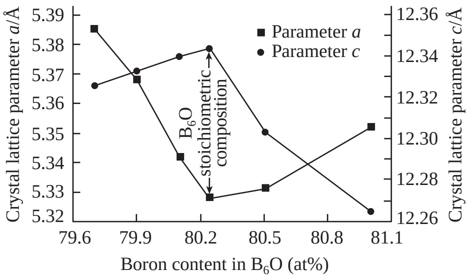

**Figure 5** Variation in the *R*3*m*-$B_6O$ lattice parameters *a* and *c* depending on the composition. Data adapted from ref. 35.

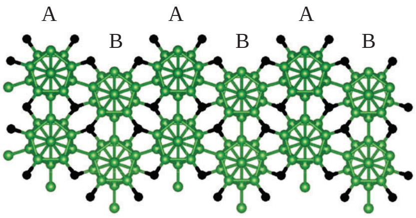

**Figure 6** Schematic diagram of atomic chains with space group *Cmcm*-$B_6O$. Green and black balls represent B and O atoms, respectively. Reproduced with permission from ref. 38. © 2018 American Chemical Society.

**Table 2** Properties of single crystals and materials based on $B_6O$, cBN, $B_4C$, and SiC.[a]

| Material | $\rho$/g cm$^{-3}$ | $\alpha$/ $10^6$ K$^{-1}$ | $\lambda$/ W m$^{-1}$ K$^{-1}$ | $\mu H$/GPa | *HV*/ GPa | Reference |
|---|---|---|---|---|---|---|
| cBN | 3.3–4.4 | 3.2 | 200–250 | 70 –80 | – | 23 |
| $B_6O$ | 2.54 | 5.6 | 18–20 | 45–50 | – | 20 |
| $B_4C$ | 2.52 | 4.6 | 32 | 42–49 | – | 40 |
| SiC | 3.21 | 4.3 | 180 | 31–36 | – | 41 |
| $B_6O$ + 5% additives | 2.45 | 5.6–6.2 | 12–18 | – | 30–36 | 20 |
| HPBC | 2.55 | 4.6–4.8 | 25–30 | – | 32–35 | 42 |
| RBBC | 2.70–2.75 | 4.3–4.6 | 30–40 | – | 26–28 | 40, 42–44 |
| LPSSiC | 3.20–3.25 | 4.8–5.2 | 80–85 | – | 21–22 | 41, 45–47 |
| SiSiC | 3.05–3.10 | 4.0–4.3 | 110–120 | – | 21–22 | 41, 48 |

[a] HPBC is hot-pressed $B_4C$ ($T$ = 1900 °C, $P$ = 50 MPa, $\tau$ = 10 min); RBBC is reaction-sintered $B_4C$ ($T$ = 1600 °C, $\tau$ = 30 min); LPSSiC is liquid-phase sintered SiC ($T$ = 1930 °C, $\tau$ = 60 min); SiSiC is reaction-sintered SiC ($T$ = 1600 °C, $\tau$ = 30 min); $\rho$ is the density; $\alpha$ is the coefficient of linear thermal expansion in a temperature range of 20–1000 °C; $\lambda$ is the thermal conductivity; $\mu H$ is the microhardness; and *HV* is the Vickers hardness.

The crystal lattice parameters of the *Cmcm*-$B_6O$ space group reported previously[34] are $a$ = 5.393, $b$ = 8.777 and $c$ = 8.736 Å.

The melting point of $B_6O$ under atmospheric pressure is 2077 °C.[39] However, $B_6O$ begins to decompose into boron and oxygen at temperatures above 2100 °C; therefore, congruent melting of this phase can be observed at high pressures only.

Table 2 compares the properties of $B_6O$ with the properties of cBN, $B_4C$, SiC, and related materials.[20,23,40–48]

## 3. Thermodynamics and phase interactions in the B–$B_2O_3$ system

The Thermo-Calc software was used[37,49] to estimate the results of X-ray powder analysis, calculate thermodynamic relationships for reactions in the B–$B_2O_3$ system, and build phase diagrams of the B–$B_2O_3$ system at pressures of 5 and 24 GPa [Figures 7(*a*),(*b*), respectively]. The melting point of boron estimated at a pressure of 5 GPa is 2440 K because the boron lines disappeared from the diffraction patterns between 2420 and 2460 K. The $B_2O_3$ phase disappeared completely at 1310 K (5 GPa). The disappearance of $B_6O$ lines at 5 GPa was observed in a range of 2670–2750 K; hence, the melting point of $B_6O$ is 2710 K.[37] In the region of eutectic compositions between $B_6O$ and $B_2O_3$ (44.9 at% B) at 5 GPa, the $B_2O_3$ phase disappeared already at 1200 K. At higher temperatures, $B_6O$ coexisted with a liquid. An increase in the temperature to 1740 K resulted in the complete disappearance of $B_6O$ lines, and the system was a homogeneous liquid phase. At this temperature, $B_6O$ dissolved in the melt of the $B_6O$–$B_2O_3$ subsystem. In a mixture of B + $B_6O$ at 5 GPa, the liquid phase appeared only at temperatures above 2460 K, which corresponds to eutectic melting in the B–$B_6O$ subsystem. At temperatures above 2100 K, the crystallization of stoichiometric $B_6O$ occurred at 1 GPa.[50]

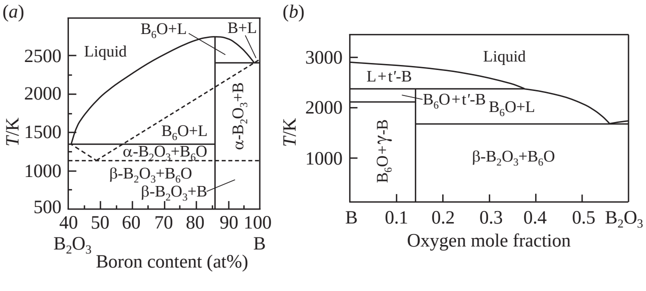

**Figure 7** Phase diagrams of the B–$B_2O_3$ system at pressures of (*a*) 5 and (*b*) 24 GPa; β, γ, and t′ are the boron allotropic forms β-$B_{106}$, γ-$B_{28}$, and t′-$B_{52}$, respectively. Reproduced with permission from ref. 49. © 2016 American Chemical Society.

The phase diagram of the B–$B_2O_3$ system at 5 GPa [Figure 7(*a*)] is characterized by the congruent melting of boron suboxide $B_6O$ and formation of two eutectic points where L + $B_2O_3$ + $B_6O$ (1290 K) and L + B + $B_6O$ (2410 K) phases coexist.

At a pressure of 24 GPa, in addition to changes in the diagram parameters (equilibrium temperature and solubility limit), the diagram topology changed and the equilibrium lines of γ-$B_{28}$ and t′-$B_{52}$ appeared. The congruent melting of $B_6O$ changed to incongruent type at pressures above 16 GPa, and L + t′-$B_{52}$ and $B_6O$ + t′-$B_{52}$ regions were formed instead of the L + $B_6O$ region [Figure 7(*b*)].

## 4. Synthesis of boron suboxide $B_6O$

The boron suboxide $B_6O$ can be synthesized using (1) a solid-phase reaction of B and $B_2O_3$ (the high vapor pressure of $B_2O_3$ during the synthesis results in an excess B concentration in boron suboxide), (2) $B_2O_3$ reduction (Si or Mg can be used as reducing agents, but they remain in the products), and (3) boron oxidation (ZnO is often used as an oxidizing agent). Table 3 summarizes methods used for the synthesis of boron suboxide.

The formation of $B_6O$ particles begins at temperatures above 1250 °C. Totally crystalline $B_6O$ is formed at 1400 °C in 1 h at the ratio of starting components B/$B_2O_3$ = 14–16 (Figure 8). However, the synthesis of boron suboxide from a B + $B_2O_3$ mixture is accompanied by the formation of a small $H_3BO_3$ impurity in the products due to a reaction of the residual $B_2O_3$ with wash water.[59] An increase in the synthesis time and temperature only results in the growth of boron suboxide grains. A temperature of 1400 °C and a time of 1 h are sufficient for the synthesis of crystalline $B_6O$.

**Table 3** Parameters of boron suboxide $B_6O$ synthesis.[33]

| Synthesis method | Starting components | Reference |
|---|---|---|
| Solid phase sintering | B + $B_2O_3$ | 51 |
| Hot pressing, solid phase sintering | B + $B_2O_3$ | 21, 25, 26, 52–54 |
| Hot pressing | B + $B_2O_3$ | 55 |
| Pulsed laser sputter deposition | B + $B_2O_3$ | 56, 57 |
| Spark plasma sintering | B + $B_2O_3$ | 58 |
| Solid phase sintering | amorphous B + α-B + $B_2O_3$ | 32, 59 |
| Reaction sintering | amorphous B + α-B + $B_2O_3$ | 60 |
| Solid phase sintering | $^{10}B$ + $^{11}B$ + $B(OH)_3$ | 61 |
| Solid phase sintering | B + $H_3BO_3$ | 62, 63 |
| Solid phase sintering | $B_2O_3$ + Si | 64 |
| Plasma arc synthesis | $B_2O_3$ + Mg | 35 |
| Sintering in air | B + ZnO | 65 |
| Reaction sintering | B + ZnO | 66 |
| Hot pressing | B + ZnO | 28 |
| Solid phase sintering | amorphous B + ZnO | 30 |

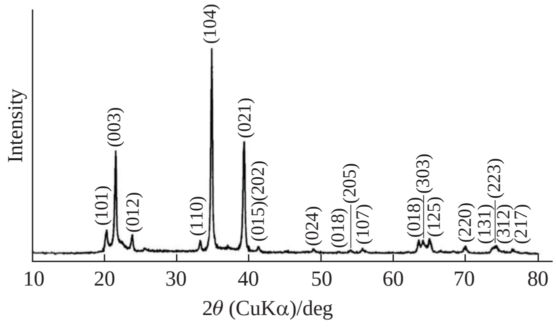

**Figure 8** X-ray diffraction pattern of $B_6O$ powder. Reproduced with permission from ref. 33. © 2002 Japan Institute of Metals.

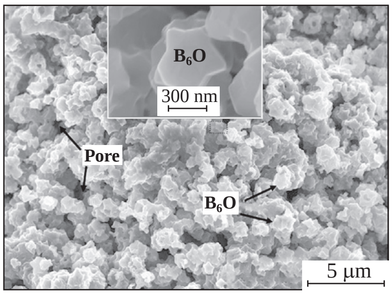

**Figure 9** Microstructure of $B_6O$ powder. Reproduced with permission from ref. 67. © 2016 Elsevier.

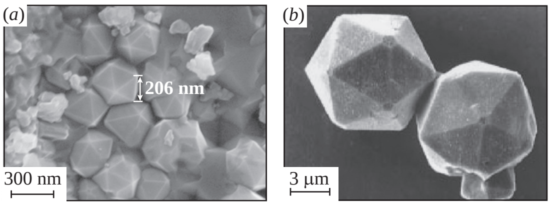

**Figure 11** Micrographs of $B_6O$ crystals: (*a*) nanosized icosahedral particles[54] and (*b*) two microsized crystals oriented along a threefold or fivefold axis.[26] Reproduced with permission from ref. 54. © 2010 Elsevier. Reproduced with permission from ref. 26. © 1998 American Chemical Society.

The microstructure of $B_6O$ is represented by star-shaped plates with sizes ranging from 0.5 to 2.0 μm (provided that the size of the starting components is 2–5 μm) (Figure 9).

The $B_6O$ powder obtained at a stoichiometric ratio between the components is deficient in oxygen due to partial evaporation of $B_2O_3$ during the synthesis.[59] The use of a larger $B_2O_3$ content of the starting mixture increases the oxygen content of the resulting powder. Treatment with a 1 M solution of HCl followed by washing with ethanol[68] decreases the oxygen content. The presence of a $B_2O_3$ impurity in $B_6O$ powders decreases the crystallite size and increases the specific surface area.

Large crystals of $B_6O$ (>1 mm) were grown by loading the initial powders into containers (Figure 10). Sintering was performed at a temperature above 1900 °C and a pressure of no lower than 5.0 GPa. The higher the sintering temperature, the larger the size of the resulting $B_6O$ crystals. An increase in the temperature enhances diffusion. As a result, atoms pass longer distances, which favors the growth of $B_6O$ crystals.[63] At 2100 °C, $B_6O$ crystals can intergrow and thus act as a barrier to further crystal growth.[53] For this reason, it is hard to obtain large $B_6O$ crystals from a mixture of B and $B_2O_3$ powders.

The formation of boron suboxide can be described as follows: boron dissolves in a $B_2O_3$ melt to give a $B_6O$–$B_2O_3$ eutectic melt. As the boron suboxide content increases, the $B_6O$–$B_2O_3$ melt becomes supersaturated with $B_6O$, and the latter is crystallized from the melt. According to He *et al.*,[53] the $B_2O_3$ impurity can be completely removed by refluxing boron suboxide crystals in deionized water for 2 h. The resulting boron suboxide has the form of transparent ruby-red crystals mixed with a very fine orange-red $B_6O$ powder.

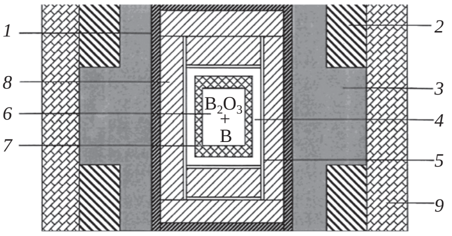

**Figure 10** Diagram of loading the starting powders ($B + B_2O_3$) into containers for growing $B_6O$ crystals at high temperature under high pressure: (*1*) graphite heater; (*2*) steel ring; (*3*) NaCl + 10 wt% $ZrO_2$ (mixture under pressure); (*4*) Ta capsule; (*5*) Ta foil; (*6*) mixture of $B + B_2O_3$ powders; (*7*) h-BN capsule; (*8*) NaCl + 20 wt% $ZrO_2$ (mixture under pressure); and (*9*) pyrophyllite shell. Reproduced with permission from ref. 53. © 2002 Materials Research Society.

The presence of a $B_2O_3$ admixture in the formation and growth of $B_6O$ begins only on the surface of boron particles. An increase in the synthesis pressure with unchanged temperature and synthesis time results in a decrease in the size of $B_6O$ crystals. The color of $B_6O$ crystals changes from orange-red to dark red with the temperature and synthesis time. The color can vary due to an oxygen admixture in $B_6O$ crystals.[53] Figure 11 demonstrates nearly ideal icosahedral $B_6O$ crystals up to 10 μm in size.[26,54]

A material based on $B_6O$ reduces the density and mechanical strength of a composite.[68–70] Boron suboxide is readily oxidized to adversely affect the properties.

## 5. Properties of dense materials based on $B_6O$

The mechanical characteristics of boron suboxide obtained from amorphous boron and $B_2O_3$ (in the ratio $\alpha$-B : $B_2O_3$ = 10 : 1) were studied by microwave sintering (MWS), hot pressing (HP), and spark plasma sintering (SPS).[67]

Covalent $B_6O$ is compacted already at a temperature of 1300 °C due to the sliding of particles and sintering along grain boundaries. At 1500 °C, weak surface diffusion begins, and rounded grains with a small number of acute-angled grains are formed.[67,71] Already at 1700 °C, dense ceramic samples are produced by the MWS method (94.2% of the theoretical density) (Table 4). Due to uniform heating upon SPS, the $B_6O$ samples had no macroscopic cracks, which usually occur in the microstructure of materials based on $B_4C$.[43,72] Materials produced by SPS feature a compaction mechanism similar to that of MWS. Table 4 summarizes the properties of the materials.

A material containing many large $B_6O$ grains undergoes transcrystalline destruction, whereas a material containing a large number of small $B_6O$ grains shows intercrystalline (intergranular) destruction resulting in tear-off of such boron suboxide grains from the matrix (Figure 12). Stronger transcrystalline fracture is observed in materials sintered at a higher temperature. In this case, in materials with small grains, the crack propagation/deflection mechanism is predominantly observed[73–75] that

**Table 4** Physical and mechanical properties of $B_6O$ materials.

| Preparation method | Synthesis temperature/°C | Exposure time/min | Relative density (%) | Grain size/μm | Flexural strength/MPa | Fracture viscosity/ MPa m$^{0.5}$ | Reference |
|---|---|---|---|---|---|---|---|
| MWS | 1700 | 5 | 94.2 ± 0.6 | 0.9 ± 0.3 | 286 ± 33 | 1.8 ± 0.1 | 67 |
| MWS | 1800 | 5 | 96.7 ± 0.4 | 1.1 ± 0.3 | 314 ± 13 | 1.7 ± 0.3 | 67 |
| MWS | 1850 | 5 | 98.1 ± 0.5 | 1.4 ± 0.5 | 405 ± 15 | 2.5 ± 0.2 | 67 |
| MWS | 1900 | 0 | 96.2 ± 0.3 | 1.3 ± 0.4 | 340 ± 10 | 2.9 ± 0.3 | 67 |
| HP | 1800 | 5 | 98.2 | 1.2 | 293 ± 15 | 2.7 ± 0.2 | 76 |
| SPS | 1800 | 1 | 98.6 | <1.6 | 300 ± 25 | 2.5 ± 0.15 | 77, 78 |
| SPS | 1900 | 5 | 99.1 | 0.26 | 410 ± 30 | 1.9 ± 0.2 | 79 |

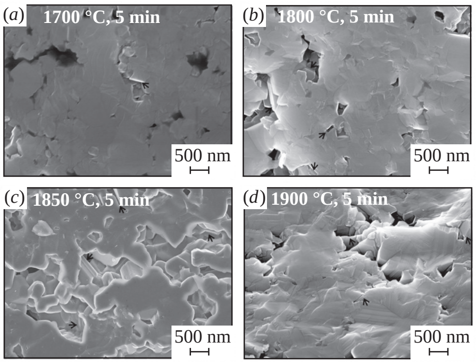

**Figure 12** Fractograms of the surfaces of boron suboxide ceramics after fracture in a strength test. Arrows show the transcrystalline destruction of $B_6O$ grains. Reproduced with permission from ref. 67. © 2016 Elsevier.

corresponds to an increase in the crack resistance of materials and a decrease in their strength (see Table 4).

The $B_6O$ ceramics achieved a flexural strength (290–420 MPa) comparable to that of monolithic boron carbide ceramics.[42,48,72] The best properties of the materials prepared by MWS at 1850 or 1900 °C for 5 min were $\sigma_{\text{flex}} = 405 \pm 15$ or $410 \pm 30$ MPa and $K_{1C} = 2.5 \pm 0.2$ or $1.9 \pm 0.2$ MPa m$^{0.5}$, respectively.

The hardness of the materials obtained by SPS reached 43 GPa at a load of 9.8 N and 28 GPa at a load of 198 N.[80] The $B_6O$ materials obtained by hot pressing at 1600 °C in a vacuum at a pressure of 40 MPa[76] have a high microhardness of 35–40 GPa, an ultimate bending strength up to 387 MPa, and a fracture viscosity up to 3.12 MPa m$^{0.5}$ (Table 5).

According to Herrmann *et al.*,[20] the single-crystal $B_6O$ obtained at a high pressure had a microhardness of 45–55 GPa and a fracture viscosity of 4.5 MPa m$^{0.5}$, while the polycrystalline material obtained at a high pressure had a microhardness of 40–43 GPa and a fracture viscosity of no higher than 2 MPa m$^{0.5}$.

**Table 5** Properties of hot-pressed $B_6O$.[72]

| Material preparation conditions | Density/ g cm$^{-3}$ | Micro-hardness/ GPa | Fracture viscosity/ MPa m$^{0.5}$ | Flexural strength/ MPa | Synthesized phases |
|---|---|---|---|---|---|
| 2 h HP | 2.15 | 35 | 1.35 | 157.18 | $B_6O$, B, and $B_2O_3$ |
| 4 h HP | 2.18 | 35 | 1.52 | 159.07 | $B_6O$, B, and $B_2O_3$ |
| 2 h HP and thermal treatment | 2.31 | 36 | 1.84 | 262.43 | $B_6O$ and B |
| 4 h HP and thermal treatment | 2.39 | 37 | 2.23 | 266.70 | $B_6O$ and B |
| 4 h HP, thermal treatment and soaking | 2.53 | 40 | 3.12 | 386.88 | $B_6O$, $Al_2O_3$, and $Al_{1.67}B_{22}$ |

The single crystals of $B_6O$ (60–140 μm in size) were synthesized in 1 h at 5.5 GPa and 2100 °C.[16] The Vickers hardness was in ranges of 48–59, 42–62 and 40–51 GPa at loads of 0.25, 0.49 and 0.98 N, respectively. The mean values of *HV* were 54, 53 and 45 GPa at loads of 0.25, 0.49 and 0.98 N, respectively. The averaged fracture viscosity was 4.5 MPa m$^{0.5}$, which agrees with values obtained previously.[20,81–83] The fracture viscosities of cBN single crystals[84–86] and diamond[87,88] are 2.8 and 5.0 MPa m$^{0.5}$, respectively. Thus, the fracture viscosity of a $B_6O$ single crystal is close to that of diamond.

## 6. Sintering of $B_6O$ with activating oxide additives

Dense materials based on $B_6O$ can be prepared by a reaction activated sintering (RAS) method based on sintering a mixture of boron and $B_2O_3$ with oxide additives, such as a yttrium aluminum garnet (YAG) mixture,[89] $ZrO_2$,[90] $Al_2O_3$,[91] $Y_2O_3$, $TiO_2$, $ZrO_2$, $HfO_2$,[92] CaO, MgO,[93] *etc*., and a non-reaction activated sintering (NRAS) method based on sintering a pre-synthesized boron suboxide powder with oxide additives.

The starting mixtures for reaction activated sintering were calculated from the reaction

$$16\,B + B_2O_3 \rightarrow 3\,B_6O,\ \Delta G = -527\ \text{kJ mol}^{-1}. \qquad (1)$$

Table 6 summarizes the density, porosity, and phase compositions of sintered materials.

The compaction of $B_6O$ without additives begins at 1540 °C to reach a relative density of 89% with respect to a theoretical value (Figure 13). According to published data,[79,94,95] the almost complete compaction of $B_6O$ (relative density, 99.1%) can be achieved by FAST/SPS at a sintering temperature of 1900 °C. However, the sintering of $B_6O$ without additives is difficult to control due to $B_6O$ decomposition at high temperatures and strong interactions with the graphite of the dies.

The addition of YAG to $B_6O$ obtained by the NRAS method lowered the initial temperature of compaction to 1410 or 1320 °C (with 3 or 6 vol% YAG, respectively), increased the compaction rate, and resulted in totally compacted materials (see Table 6).

Figures 14 and 15 show the results of the DTA/TG analysis of the material obtained by non-reactive activated sintering and reaction activated sintering, respectively, with 6 vol% YAG and without additives. The thermogravimetric characteristics (Figure 14) show a weight loss of about 1% up to 550 °C, which is accompanied by a broad endothermic effect due to the decomposition of a partially hydrated $B_2O_3$ layer (consisting of $H_3BO_3$) on the surface of $B_6O$ particles.

The evaporation of $B_2O_3$ begins at temperatures above 1000 °C and causes a further slow but continuous mass loss (see

**Table 6** Properties of sintered materials based on $B_6O$.[89]

| Composition | Starting composition (wt%) | | | | | Total amount of additives (vol%) | Density/ g cm$^{-3}$ | Porosity (%) | Phase composition of sintered materials |
|---|---|---|---|---|---|---|---|---|---|
| | $B_6O$ | B | $B_2O_3$ | $Al_2O_3$ | $Y_2O_3$ | | | | |
| NRAS-0 | 100 | – | – | – | – | – | 2.27 | 10.6 | $B_6O$ |
| NRAS-3 | 94.7 | – | – | 2.3 | 3.0 | 3.0 | 2.59 | 0 | $B_6O$, YAB, $AlB_{31}$ |
| NRAS-6 | 89.8 | – | – | 4.4 | 5.8 | 6.0 | 2.63 | 0 | $B_6O$, YAB, $AlB_{31}$, $YB_{12}$, (Y, Al)-boride |
| RAS-0c | – | 70.7 | 29.3 | – | – | – | 2.43 | 5.0 | $B_6O$, $B_2O_3$ |
| RAS-0n | – | 75.6 | 24.4 | – | – | – | 2.09 | 17.7 | $B_6O$, $B_2O_3$ |
| RAS-3s | – | 67.2 | 27.8 | 2.1 | 2.9 | 2.9 | 2.49 | 1.5 | $B_6O$, YAB, $B_2O_3$ |
| RAS-6s | – | 63.5 | 26.3 | 4.5 | 5.7 | 6.1 | 2.57 | 0.5 | $B_6O$, YAB |
| RAS-6n | – | 67.8 | 22.0 | 4.4 | 5.8 | 6.0 | 2.62 | 0.5 | $B_6O$, YAB, $AlB_{31}$, $YB_{12}$, (Y, Al)-boride |

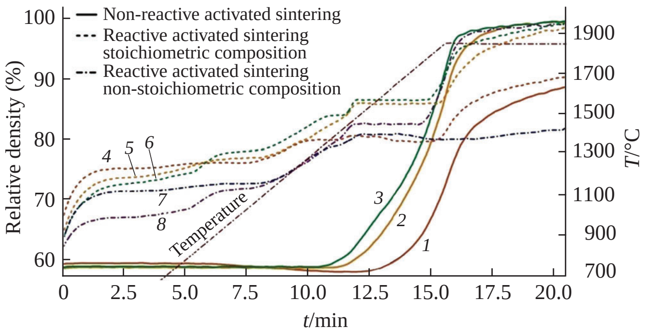

**Figure 13** FAST/SPS compaction curves: (*1*) $B_6O$ obtained by non-reaction activated sintering without oxide additives (NRAS-0); (*2*) $B_6O$ obtained by non-reaction activated sintering with addition of 3 vol% YAG (NRAS-3); (*3*) $B_6O$ obtained by non-reaction activated sintering with addition of 6 vol% YAG (NRAS-6); (*4*) stoichiometric $B_6O$ obtained by reaction activated sintering without oxide additives (RAS-0s); (*5*) $B_6O$ with non-stoichiometric composition obtained by reaction activated sintering without oxide additives (RAS-0n); (*6*) stoichiometric $B_6O$ obtained by reaction activated sintering with addition of 3 vol% YAG (RAS-3s); (*7*) stoichiometric $B_6O$ obtained by reaction activated sintering with addition of 6 vol% YAG (RAS-6s); and (*8*) $B_6O$ with non-stoichiometric composition obtained by reaction activated sintering with addition of 6 vol% YAG (RAS-6n). Reproduced with permission from ref. 89. © 2015 Elsevier.

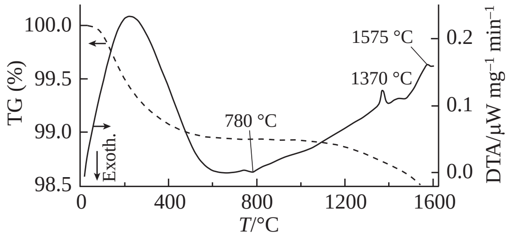

**Figure 14** DTA/TG curves of the NRAS-6 material. Reproduced with permission from ref. 89. © 2015 Elsevier.

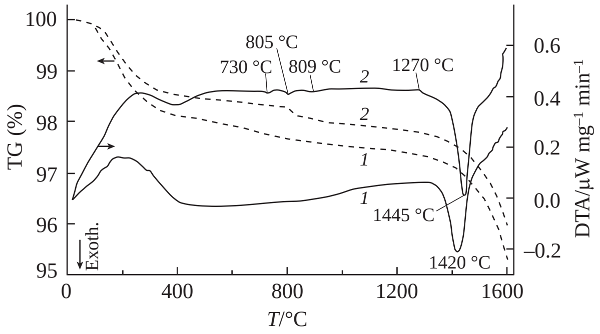

**Figure 15** DTA/TG curves of (*1*) RAS-0s and (*2*) RAS-6s materials. Reproduced with permission from ref. 89. © 2015 Elsevier.

Figure 14). Three effects are observed on DTA curves: a weak exothermic effect at 780 °C corresponding to the formation of a $Y_2O_3$–$Al_2O_3$–$B_2O_3$ glass and two endothermic effects at 1370 °C due to the synthesis of yttrium aluminum garnet (YAG) followed by partial disappearance of the $Y_2O_3$–$Al_2O_3$–$B_2O_3$ glass at 1575 °C. As found previously,[64,70] the intense formation of volatile gaseous components (mainly $B_2O_2$) occurred at temperatures above 1750 °C due to the $B_6O$ decomposition:

$$2\,B_6O \rightarrow 10\,B + B_2O_2\uparrow,\ \Delta G = 580\ \text{kJ mol}^{-1}, \qquad (2)$$

and

$$B_6O + 5\,B_2O_3 \rightarrow 8\,B_2O_2\uparrow,\ \Delta G = 3238\ \text{kJ mol}^{-1}. \qquad (3)$$

Intense compaction begins relatively late at temperatures above 1300 °C, but a continuous density increase is observed up to the sintering temperature (see Figure 13).

Abnormal growth of $B_6O$ grains in the $B_6O + 6$ vol% YAG composition obtained by the NRAS method begins at about 2000 °C. After that, a large amount of liquid $Y_2O_3$–$Al_2O_3$–$B_2O_3$ begins to evolve with a subsequent temperature rise to 2050–2100 °C. The final sintered body consists of $B_6O$ and a large amount of a $Y_2O_3$–$Al_2O_3$–$B_2O_3$ glass.

The compaction curves of $B/B_2O_3$ materials show a high compaction rate up to 500 °C, which is explained by $B_2O_3$ melting at a temperature of about 450 °C (see Figure 13). The small $B_2O_3$ content of the materials obtained by RAS results in a smaller compaction rate in this temperature range than that in the materials obtained by NRAS. After low-temperature compaction of pure $B/B_2O_3$ formulations, further compaction is observed in a temperature range of 1100–1500 °C. The DTA/TG analysis of the stoichiometric $B/B_2O_3$ material (Figure 15) shows an exothermic effect at 1420 °C due to the beginning of $B_6O$ crystallization from the initial mixture of amorphous boron and $B_2O_3$ (Figure 16). The TG analysis reveals a mass decrease during the exothermic reaction, which results from the evaporation of a fraction of $B_2O_3$ caused by a local temperature increase due to the strong exothermic reaction (see Figure 15). Powder X-ray analysis proves that, already at 1400 °C, $B_2O_3$ is completely consumed for the formation of $B_6O$ in stoichiometric materials obtained by the RAS method (see Figure 16).

The DTA curve of stoichiometric $B_6O$ material prepared by RAS with the addition of 6 vol% YAG shows three weak exothermic peaks at 730 °C (due to the formation of a $Y_2O_3$–$Al_2O_3$–$B_2O_3$ glass), 805 and 890 °C (due to the formation of $Al_4B_2O_9$ and $Al_{18}B_4O_{33}$) (see Figure 15). The material mass begins to decrease at 805 °C (TG curve, Figure 15). The temperature of $B_6O$ formation from a $B/B_2O_3$ mixture without additives is slightly lower (1420 °C) than the synthesis temperature of boron suboxide with the addition of 6 vol% YAG (1445 °C). The compaction of such materials is completed at 1950 and 1700 °C, respectively (see Figure 13). The use of sintering additives makes it possible to obtain materials with high density and negligible porosity (see Table 6).

The large ratio $B_2O_3/(Al_2O_3 + Y_2O_3)$ in these materials results in a high porosity compared to materials obtained by the NRAS method due to enhanced formation of volatile $B_2O_2$ and decomposition products of $B_6O$. Therefore, a high activity of $B_2O_3$ and a low activity of $Al_2O_3$ and $Y_2O_3$ reduce the amount of borides formed upon sintering, while a low activity of $B_2O_3$ and a high activity of $Al_2O_3$ and $Y_2O_3$ shift the reaction equilibriums to the right with the formation of borides:

$$Al_2O_3 + 12\,B_6O \rightleftarrows 5\,B_2O_{3(L)} + 2\,AlB_{31}. \qquad (4)$$

According to Figures 14 and 15, $B_2O_3$ gradually evaporates or decomposes during sintering. Hence, a decrease in the concentration of $B_2O_3$ results in the formation of borides *via*

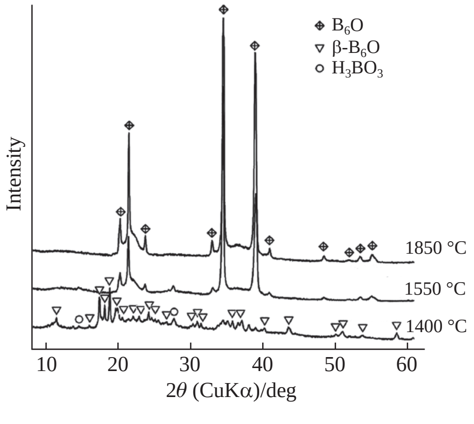

**Figure 16** Powder XRD patterns of a stoichiometric $B/B_2O_3$ mixture (RAS-0s) at various sintering temperatures.

reaction (4). With a further temperature increase, $B_2O_3$ decomposes and crystallization of $B_6O$ begins.

Thermodynamic calculations show[70] that, at low temperatures, carbon reacts with $B_2O_3$ to give $B_6O$:

$$8C + 3B_2O_3 \rightarrow B_6O + 8CO\uparrow. \tag{5}$$

This reaction strongly depends on the partial pressure of CO, which reaches 1 atm at temperatures above 1544 °C. As a result, $B_2O_3$ and carbon vigorously react to give $B_6O$. Carbon can also react with $B_6O$ to afford boron carbide:

$$2B_6O + 5C \rightarrow 3B_4C + 2CO\uparrow. \tag{6}$$

At 1616 °C, the partial pressure of CO exceeds 1 atm, and the excess carbon begins to reduce boron suboxide to $B_4C$ after complete decomposition of $B_2O_3$. Accordingly, at sintering temperatures above 1616 °C (hot pressing), $B_4C$ was present in the synthesis products.

Note that boron suboxide reacts with the complex oxide $Al_2O_3 + B_2O_3$ in the course of sintering. This favors the evaporation of a liquid phase and the formation of gaseous $B_2O_2$:

$$2B_6O + 5(Al_2O_3 + B_2O_3)_{(L)} \rightarrow 6B_2O_2\uparrow + 10BAlO_2. \tag{7}$$

Thermodynamic calculations have shown that the amount of the liquid phase during sintering depends on the $B_2O_3$ and $Al_2O_3$ content, which strongly affects the compaction.

Figure 17(*a*) shows a micrograph of a sintered $B_6O$ material (NRAS method) with an admixture of 6 vol% YAG. Apart from $B_6O$ grains and an amorphous glass phase in the $Y_2O_3$–$Al_2O_3$–$B_2O_3$ system, the microstructure included boride phases with the outer edge of $AlB_{31}$ and a core of cubic $YB_{12}$ or mixed Y–Al boride. The total amount of Y + Al was about 3–4 at% of the concentration of borides.

Figure 17(*b*) shows a micrograph of a sintered $B_6O$ material (RAS method) containing no admixtures. The $B_6O$ grains had irregular shapes; the pores (100–200 nm in diameter) were uniformly distributed in the material structure. The pores were partially filled with unreacted residual $B_2O_3$. The addition of 3 and 6 vol% YAG [Figures 17(*c*),(*d*), respectively] resulted in the formation of amorphous phases ($B_2O_3$ and $Y_2O_3$–$Al_2O_3$–$B_2O_3$ glasses) uniformly distributed in a matrix of the $B_6O$ material. If 3 vol% YAG was added, an amorphous two-layer phase comprising a core with a high $B_2O_3$ content [glass A, Figure 17(*c*)] and a glass shell in the $Y_2O_3$–$Al_2O_3$–$B_2O_3$ system [glass B, Figure 17(*c*)] were formed. In materials with 6 vol% YAG, a homogeneous glass in the $Y_2O_3$–$Al_2O_3$–$B_2O_3$ system was formed along with a phase of $AlB_{31}$ located along the outer edge of the pores [Figure 17(*d*)].

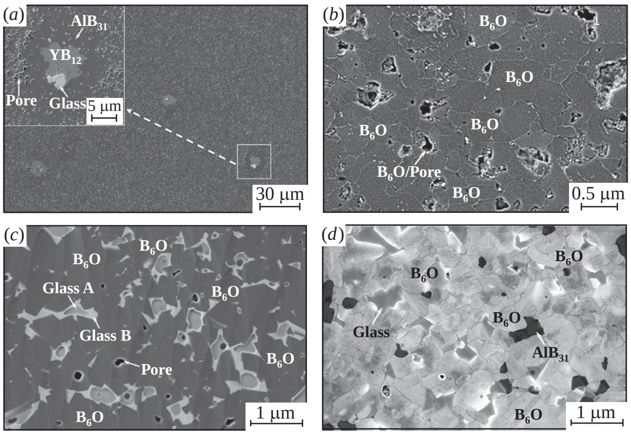

**Figure 17** Micrographs of sintered $B_6O$ materials: (*a*) obtained by the NRAS method with addition of 6 vol% YAG; (*b*) obtained by the RAS method without additives; (*c*) obtained by the RAS method with addition of 3 vol% YAG; and (*d*) obtained by the RAS method with addition of 6 vol% YAG. Reproduced with permission from ref. 67. © 2016 Elsevier.

**Table 7** Mechanical properties of FAST/SPS sintered materials based on $B_6O$.[89]

| Material | Flexural strength/MPa | Fracture viscosity/ MPa m$^{0.5}$ | Vickers hardness/ GPa |
|---|---|---|---|
| NRAS-3 | 540 ± 50 | 3.0 ± 0.3 | 24.5 ± 0.3 |
| NRAS-6 | 350 ± 20 | 2.8 ± 0.4 | 22.3 ± 0.2 |
| RAS-0s | – | – | 16.6 ± 2.7 |
| RAS-3s | 360 ± 50 | 3.0 ± 0.4 | 18.1 ± 1.8 |
| RAS-6s | 230 ± 10 | 2.8 ± 0.2 | 19.4 ± 0.5 |
| RAS-6n | 250 ± 20 | 2.6 ± 0.1 | 21.5 ± 1.2 |

The hardness of materials obtained by the RAS method depends on the residual porosity and gradually increases with the amount of sintering additives (Table 7). The hardness of the material with the addition of 6 vol% YAG (a stoichiometric composition) was smaller than that of a non-stoichiometric material. The hardness of materials obtained by the NRAS method with nearly zero porosity is determined by the amount of softer (oxide) phases.[20,95]

The materials obtained by the RAS method show a comparatively low strength, though they contain no borides, which reduce the strength.[94] An increase in the amount of additives significantly reduced the strength of non-reactive sintered formulations (see Table 7).

Regardless of the preparation mode, the materials had equal fracture viscosity values of about 3.0 MPa m$^{0.5}$ even with different amounts of oxide additives[20,94,96] (see Table 7).

The compaction of $B/B_2O_3$ containing $ZrO_2$ or $B_6O$ containing $ZrO_2$ was caused by the formation of $ZrB_2$ in the final product[85] due to the reduction of zirconium dioxide with boron or $B_6O$. A similar process was observed upon the sintering of $B/B_2O_3$ or $B_6O$ with $TiO_2$[89] or other oxides ($HfO_2$ and $WO_3$).[92] The Vickers hardness of $B_6O$ materials with a low $ZrB_2$ content varied from 26 to 32 GPa, and that of materials with a high $ZrB_2$ content was in a range of 21–30 GPa.[59,89]

In addition to the crystalline phase of $B_6O$, various phases were formed upon the sintering of boron suboxide with alkaline earth metal oxide additives: $Mg_2B_2O_5$ (sintering with MgO), $CaB_6$ (with CaO), and $B_4C$ and $CaB_6$ (with $CaCO_3$). The $B_4C$ phase can be formed due to carbon capture in a reaction with $CaCO_3$ or the saturation of material with carbon from the graphite die.[92]

The nonuniform liquid distribution in $B_6O$ materials sintered with CaO and $CaCO_3$ additives results from the poor wettability of boron suboxide, which leads to the sintering (hot pressing) of a high-porosity material (Table 8). The following reactions occurred in the course of the hot pressing of such materials:

$$4CaO + 5B_6O \rightarrow 4CaB_6 + 3B_2O_3\uparrow, \tag{8}$$

$$4CaCO_3 + 9B_6O \rightarrow 4CaB_6 + 4B_4C + 7B_2O_3\uparrow. \tag{9}$$

Table 8 gives the properties of hot-pressed $B_6O$ materials with alkaline earth metal oxide additives.[97] Except for a

**Table 8** Properties of hot-pressed $B_6O$ materials with alkaline earth metal oxide additives.

| Material | Density/ g cm$^{-3}$ | Relative density (%) | Open porosity (%) | Vickers hardness/ GPa | Fracture viscosity/ MPa m$^{0.5}$ |
|---|---|---|---|---|---|
| $B_6O$ + 1.4 wt% CaO | 2.44 | 95.3 | 1.45 | 32.1 ± 1.9 | 6.8 ± 1.6 |
| $B_6O$ + 1.5 wt% MgO | 2.51 | 98.0 | 0.86 | 31.6 ± 2.1 | 6.1 ± 1.3 |
| $B_6O$ + 0.7 wt% $CaCO_3$ | 2.50 | 97.7 | 0.97 | 31.6 ± 1.7 | 6.1 ± 1.7 |

material with CaO added, whose density is low, the density of $B_6O$–alkaline earth metal oxide ceramics is higher than that of boron suboxide without additives. Pores in the material can be due to the evaporation of $B_2O_3$ at high temperatures.[20,92,98] Generally, the addition of small amounts of alkaline earth metal oxides results in a significant increase in the fracture viscosity compared to that of $B_6O$ without additives. The material underwent destruction mainly by a transcrystalline mechanism.

## 7. Performance characteristics of $B_6O$ materials

*High-temperature and thermophysical properties*

Figure 18 shows the temperature dependence of the flexural strength of a material based on $B_6O$ obtained by SPS. Brittle fracture of the material was predominant in high-temperature flexural strength tests.

At temperatures to 1000 °C, the strength of single-crystal $B_6O$ increased from 310 to 360 MPa; with a further increase in the temperature to 1400 °C, a stronger increase in the strength to 440 MPa was observed, followed by a sharp decrease in the strength.[78]

At room temperature, the destruction of the material was mainly determined by its intercrystalline nature (a weaker intergranular phase), and it was accompanied by the tear-out of grains from the intergranular phase. Moreover, isolated instances of the transcrystalline destruction of grains were observed (see Figure 12). However, at temperatures above 1000 °C, larger amounts of a glassy viscous phase appeared to result in an increase in the contribution of plastic deformation to fracture stress, an increase in the transcrystalline nature of fracture, and, accordingly, an increase in bending strength (see Figure 18).

This behavior is not typical of materials based on boron carbide[99] or silicon carbide[100] whose destruction mainly occurs in intercrystalline mode.

At temperatures above 1400 °C, the viscosity of the glassy intergranular phase (based on $B_2O_3$) decreased and the material weakened.

Figure 19 shows the temperature dependence of hardness. The coefficient of thermal linear expansion of $B_6O$ without additives at 1000 °C was $5.6\times10^{-6}$ $K^{-1}$, and it increased to $6.2\times10^{-6}$ $K^{-1}$ in $B_6O$ sintered with oxide additives.[101]

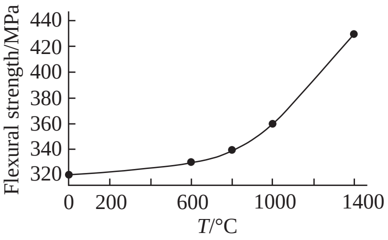

**Figure 18** Plot of flexural strength *vs.* temperature for a $B_6O$ material. Data adapted from ref. 78.

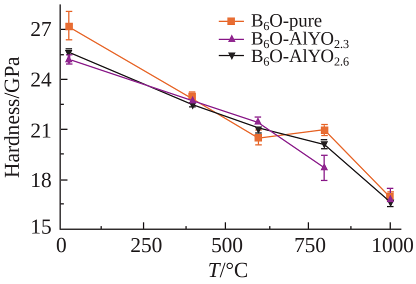

**Figure 19** High-temperature hardness of materials based on $B_6O$. Reproduced with permission from ref. 101. © 2011 Elsevier.

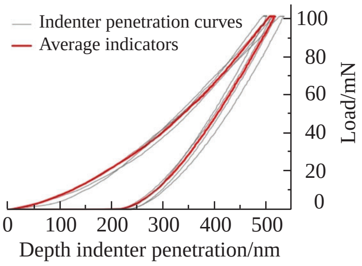

**Figure 20** Load–indenter penetration curves for hot pressed $B_6O$ measured under nanoindentation at room temperature. Reproduced with permission from ref. 102. © 2014 Elsevier.

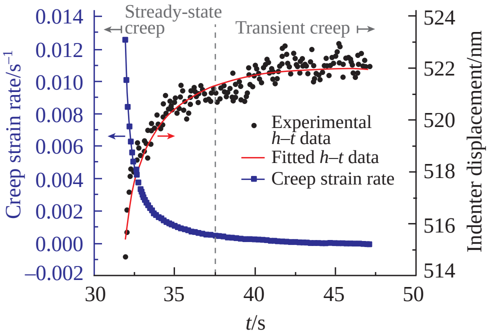

**Figure 21** Typical creep–time curve (*h*–*t* curve) under nanoindentation of hot-pressed $B_6O$. Reproduced with permission from ref. 102. © 2014 Elsevier.

Figures 20 and 21 show load–indenter penetration curves for hot-pressed $B_6O$ measured at room temperature[102] and a typical creep displacement time curve measured under nanoindentation, respectively.

Accordint to Figure 21, the initial stage of creep is relatively short, and it is characterized by unstable creep with a rapidly decreasing creep strain rate. The next stage is characterized by stable creep (constant creep strain rate $\varepsilon \to 0$ in the case of $B_6O$); strain hardening and reduction can occur as competing creep mechanisms.[103] It can be concluded that a material based on $B_6O$ with a small amount of sintering additives is totally resistant to creep.

The thermal conductivity of stoichiometric $B_6O$ at room temperature is 200 W $m^{-1}$ $K^{-1}$ and that of $B_{6.65}O$ is slightly smaller. The thermal conductivity of the material decreases with the operating temperature.

Figure 22 shows the temperature dependence of the thermal conductivity of hot-pressed $B_6O$[33] and $B_4C$.[104] The thermal conductivity decreased with temperature due to the predominance of phonon diffusion.[105] The thermal conductivity of $B_6O$ strongly decreased with increasing porosity. The thermal conductivity of

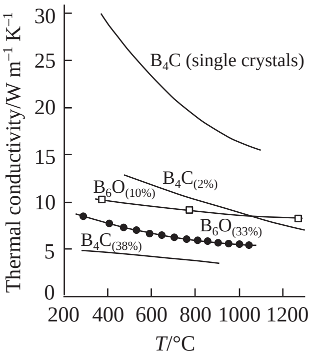

**Figure 22** Temperature dependence of the thermal conductivity coefficient of hot-pressed $B_6O$. The numbers in parentheses indicate the porosity of samples. Reproduced with permission from ref. 33. © 2002 Japan Institute of Metals.

boron suboxide was higher than that of boron carbide at the same porosity of the materials.

### *Semiconductive and thermoelectric properties*

Boron suboxide $B_6O$ is a stable semiconductor in which each oxygen atom donates four electrons, as it is typical of *p*-elements. To enhance the semiconductive properties of boron suboxide, a fraction of oxygen is replaced by boron. This state can be described by the formula $B_{6.65}O$. This boron suboxide has the same concentration of *p*-type carriers as boron carbide $B_{4.3}C$.[39]

The band gap of $B_6O$ is 2.5 eV.[104] The ZT value of hot-pressed $B_6O$ increases with temperature to reach $0.62\times10^{-3}$ at 1000 K. The ZT value of $B_{6.65}O$ at 1200 °C is 0.2, which is higher than that of $B_{4.3}C$ by a factor of 6. It is possible to assume that $B_6O$ can be used as a thermoelectric material. Moreover, boron suboxide is more heat resistant than boron carbide.[39]

The positive Seebeck coefficient of $B_6O$ means that holes serve as electron carriers in $B_6O$. The Seebeck coefficient of $B_6O$ increases with temperature to reach 500 $\mu V\ K^{-1}$ at 1000 K.[33]

The electrical conductivity of $B_6O$ increases with temperature, and it is $1.1\times10^2$ S at 1020 K.

The Hall mobility of charge carriers in $B_6O$ increases from $1\times10^{-5}$ to $1\times10^{-4}\ m^2\ V^{-1}\ s^{-1}$ with an increase in temperature from 290 to 800 K. The low mobility and its positive temperature dependence are indicative of jump conductivity. The activation energy of boron suboxide (0.09 eV) is higher than that of boron carbide (0.05 eV). The concentration of holes in $B_6O$ is smaller than that in $B_4C$, which justifies that the Seebeck coefficient is larger than that of $B_4C$.

### *Oxidation stability*

Figure 23 illustrates the isothermal oxidation of two ceramics based on $B_6O$.

In a humid atmosphere at 1000 °C, the mass of materials decreased with time. Moreover, the mass loss of $B_6O$ with oxide additives was smaller. The mass loss of cBN was smaller than that of $B_6O$. Single-crystal X-ray diffraction studies of $B_6O$ revealed that the material contained $B_2O_3$ formed as a crystalline phase after the oxidation of pure boron suboxide for 1 h or after the oxidation of $B_6O$ containing additives for 10 h. Additionally, $Al_5BO_9$ and yttrium aluminum borate phases were detected.[106]

Figure 24 shows the microstructures of $B_6O$ materials oxidized in humid air at 1000 °C for 10 h.

The oxide layers formed on a $B_6O$ material upon oxidation had numerous cracks due to different thermal expansion of boron suboxide and the oxide layer. The $B_6O$ materials with oxide additives obtained under wet oxidation conditions contained a large amount of a glassy surface layer.

Figure 25 shows the micrographs of $B_6O$ with oxide additives (cross-sections of materials) after 10 h of oxidation in dry and wet air.[106] The oxide layer thickness of a sample oxidized in dry air was smaller than 10 µm. The oxide layer consisted of boron and oxygen and also contained small amounts of Al, Y, and Mg.

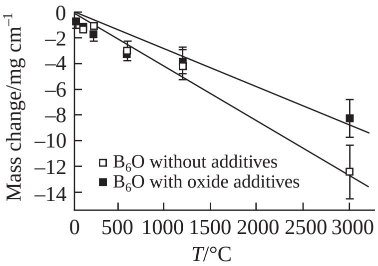

**Figure 23** Variation in the mass of $B_6O$ materials in the course of isothermal oxidation to a temperature of 1000 °C. Reproduced with permission from ref. 106. © 2011 Elsevier.

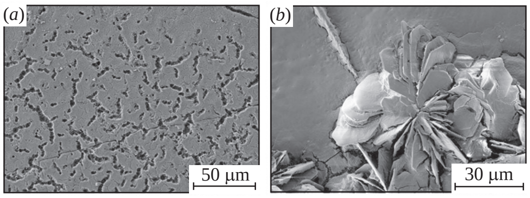

**Figure 24** Micrographs of the surfaces of $B_6O$ materials (*a*) without additives and (*b*) with sintering oxide additives after oxidaton in humid air. Reproduced with permission from ref. 106. © 2011 Elsevier.

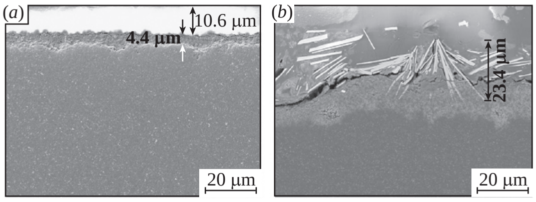

**Figure 25** Micrographs of a $B_6O$ material with oxide additives (cross section) oxidized in (*a*) dry air and (*b*) humid air. Reproduced with permission from ref. 106. © 2011 Elsevier.

The material was oxidized more strongly upon exposure to humid air. In this case, the surface layer consisted of two sublayers: an external glassy layer based on $B_2O_3$ and a layer enriched in sintering additives with a thickness of up to 10 µm.

At low temperatures, all of the samples demonstrated a small mass loss due to moisture removal and $HBO_2$ evaporation (thermodynamic calculations showed that the acid decomposes completely above 300 °C). In $B_6O$ samples oxidized in a humid atmosphere, the mass loss continued up to 750 °C. This can be due to an exposure of thin surface layers consisting of $B_2O_3$ to moisture followed by their partial removal.

A further increase in the temperature resulted in an increase in the masses of all samples regardless of the oxidizing atmosphere. This fact indicates that, during the oxidation of $B_6O$ or cBN, the mass increased in accordance with the equations

$$B_6O + 4O_2 \rightarrow 3B_2O_3,\ \Delta m = 158.2\%, \tag{10}$$

$$2BN + 1.5O_2 \rightarrow B_2O_3 + N_2,\ \Delta m = 39.2\%. \tag{11}$$

The mass of $B_6O$ increased greater than that in the oxidation of cBN[107] by a factor of approximately 4. The $B_6O$ material with sintering additives in a YAG system showed a mass gain in the first 20 min of oxidation.

On exposure to dry air, the partial pressure of boron-containing compounds is low ($1\times10^{-7}$ atm) and the oxide layer is stable. In contrast, the partial pressure of $HBO_2$ and $H_3BO_3$ in humid air at 1000 °C is about $1\times10^{-3}$ atm; therefore, the evaporation of boron-containing compounds occurs. The oxidation is determined by oxygen diffusion through the oxide layer formed, which is too thin at the beginning of oxidation. As the layer thickness increased, oxygen diffusion slowed down, and the rate of oxidation decreased. Sintering additives enriched the surface layer with a viscous oxide phase, which hindered the oxidation of the material and reduced the rates of evaporation in comparison to those in pure $B_6O$.

The oxidation resistance of cBN was higher than that of materials based on $B_6O$ by a factor of 4. Nevertheless, oxide additives can improve the oxidation resistance of boron suboxide (the oxidation resistance is 20% smaller than that of cBN) due to the formation of a glassy surface layer.[106]

## 8. Composite materials based on $B_6O$

### *Synthesis and properties of* $B_6O$*–diamond materials*

Composite materials $B_6O$–(10–80) vol% diamond were obtained in a high-pressure chamber in 20 min at *P* = 3–5 GPa and

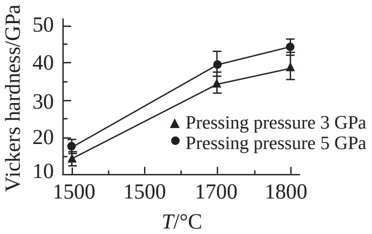

**Figure 26** Temperature dependence of the Vickers hardness of the $B_6O$–30 vol% diamond composite. Reproduced with permission from ref. 69. © 2001 Springer.

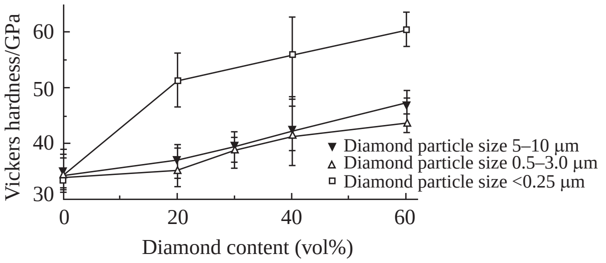

**Figure 27** Vickers hardness of sintered $B_6O$–diamond composites *vs.* the diamond content. Reproduced with permission from ref. 69. © 2001 Springer.

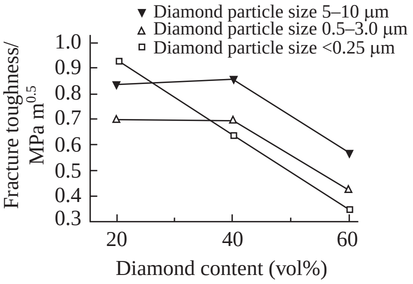

**Figure 28** Fracture viscosity of sintered $B_6O$–diamond composites *vs.* the diamond content. Reproduced with permission from ref. 69. © 2001 Springer.

1400–1800 °C.[69] If a small amount of diamond particles was used, $B_6O$ acted as a composite matrix and diamond was a reinforcing component. With a large amount of diamond particles, they acted as a matrix with the inclusions of boron suboxide particles.

Figure 26 demonstrates the temperature dependence of the Vickers hardness of a $B_6O$–30 vol% diamond composite obtained at 3 and 5 GPa. The hardness increased with the sintering temperature and compacting pressure of the composite material.[69]

Figure 27 shows the dependence of the Vickers hardness on the diamond content of the sintered composite. At a diamond particle size of >0.5 μm, the hardness of the composite increased with the diamond content to reach 45 GPa. With small diamond particles (<0.25 μm), the Vickers hardness of the $B_6O$–60 vol% diamond composite material reached 60 GPa.[69]

The effect of the diamond content of the $B_6O$–diamond composite materials on the fracture viscosity under invariable process conditions of the sintering (a pressure of 5 GPa, a temperature of 1700 °C, and an exposure time of 20 min) is shown in Figure 28. The fracture viscosity of the composites decreased if >40 vol% of diamond was used.[69]

*Synthesis and properties of $B_6O$–$B_4C$ materials*

According to Solodkyi *et al.*,[108] dense $B_6O$–$B_4C$ composite materials can be obtained by the SPS method in 1 min at pressures of 30, 60, and 80 MPa in Ar at a temperature of 1800 °C.

The relative density of the materials thus obtained increased from 96.1 to 98.3% as the pressure was increased from 60 to 80 MPa. The hardness of these composites reached 34.8 GPa, and the fracture viscosity was 4.0 MPa m$^{0.5}$.[108] The high values of hardness and crack resistance of $B_6O$–$B_4C$ composites were determined by the lower amounts of a glassy phase of $B_2O_3$ in the materials.

The compression ratio of the composite slightly decreased upon the addition of (20–40) vol% $B_4C$. The hardness decreased upon the addition of >10 vol% $B_4C$. The composite of 90 vol% $B_6O$ + 10 vol% $B_4C$ revealed the best properties: Vickers hardness, 40.8 ± 1.3 GPa and fracture viscosity, 4.8 ± 0.2 MPa m$^{0.5}$ (the measurements were performed at a load of 9.8 N).[109]

## 9. Conclusions

Of the boron suboxides, namely, $B_2O$, $B_6O$, $B_{13}O_2$, $B_7O$, and $B_{22}O$, the materials other than $B_2O$ are promising superhard materials. The suboxides are characterized by a rhombohedral α-B structure with icosahedral $B_{12}$ units bound by oxygen atoms. $B_6O$ is characterized by high hardness (up to 55 GPa measured in single crystals), low specific density (2.54 g cm$^{-3}$), good chemical inertness, and excellent wear resistance. Boron suboxide can be synthesized at atmospheric pressure, in contrast to diamond and cubic boron nitride.

Boron suboxide exists in two space groups, $R3m$-$B_6O$ and $Cmcm$-$B_6O$. Using interpolation, the crystal lattice parameters of the hexagonal unit cell of stoichiometric $R3m$-$B_6O$ (80.24 at% B) were calculated to be $a$ = 5.328 and $c$ = 12.344 Å.

The melting point of $B_6O$ at atmospheric pressure is 2077 °C, but boron suboxide begins to decompose into boron and oxygen at temperatures above 2100 °C.

The methods for synthesizing $B_6O$ include a solid-phase reaction of B and $B_2O_3$, the reduction of $B_2O_3$, and the oxidation of boron. The particles of $B_6O$ were formed at temperatures above 1250 °C. Totally crystalline $B_6O$ was formed at 1400 °C in 1 h at the ratio between starting components $B/B_2O_3$ = 4–16.

Large crystals (>1 mm) of $B_6O$ were grown at high temperatures (>1900 °C) and pressures (>5.0 GPa). The color of $B_6O$ crystals changed from orange-red to dark red with increaseing temperature and synthesis time.

The compaction of $B_6O$ without additives up to a relative density of 99.0% can be performed by the SPS method at 1900 °C; however, its stoichiometry is difficult to control due to the simultaneous decomposition of $B_6O$. This ceramic material showed the following properties: $\sigma_{\text{flex}} = 410 \pm 30$ MPa and $K_{1C} = 1.9 \pm 0.2$ MPa m$^{0.5}$. Monocrystalline $B_6O$ obtained at a high pressure had a microhardness of 45–55 GPa and a fracture viscosity of 4.5 MPa m$^{0.5}$.

The addition of YAG to $B_6O$ decreased the starting compaction temperature to 1410 or 1320 °C (at 3 or 6 vol% YAG, respectively).

The compaction of $B/B_2O_3$ containing $ZrO_2$ or $B_6O$ containing $ZrO_2$ was caused by the formation of $ZrB_2$. A similar process was observed upon the sintering of $B/B_2O_3$ or $B_6O$ with $TiO_2$, $HfO_2$, $WO_3$, *etc*. The Vickers hardness of $B_6O$ with a low $ZrB_2$ content ranged from 26 to 32 GPa.

At temperatures up to 1000 °C, the strength of monolithic $B_6O$ slightly increased from 310 to 360 MPa; at 1400 °C, the strength intensed to 440 MPa. At higher temperatures, the viscosity of a glassy intergranular phase (based on $B_2O_3$) decreased and the material weakened.

The coefficient of thermal linear expansion of $B_6O$ without additives was $5.6 \times 10^{-6}$ K$^{-1}$ at 1000 °C, and it increased to $6.2 \times 10^{-6}$ K$^{-1}$ in $B_6O$ sintered with oxide additives.

The thermal conductivity of stoichiometric $B_6O$ at room temperature was 200 W m$^{-1}$ K$^{-1}$, and it decreased with temperature.

The semiconductive properties of boron suboxide increased if a fraction of oxygen was replaced by boron ($B_{6.65}O$). The electrical conductivity of $B_6O$ was $1.1 \times 10^2$ S at 1020 K, and it increased with temperature.

The Vickers hardness of $B_6O$–diamond composites increased with temperature and compacting pressure. With small diamond particles (<0.25 μm), the Vickers hardness of the $B_6O$–60 vol% diamond material reached 60 GPa.

The 90 vol% $B_6O$ + 10 vol% $B_4C$ composite material was characterized by a Vickers hardness of $40.8 \pm 1.3$ GPa and a fracture viscosity of $4.8 \pm 0.2$ MPa $m^{0.5}$.

This study was performed with financial support from the Russian Foundation for Basic Research within the framework of scientific project no. 20-13-50002, https://kias.rfbr.ru/index.php.

## References

1 A. R. Oganov, J. Chen, C. Gatti, Y. Ma, C. W. Glass and V. L. Solozhenko, *Nature*, 2009, **457**, 863.

2 Q. An, K. M. Reddy, K. Y. Xie, K. J. Hemker and W. A. Goddard III, *Phys. Rev. Lett*., 2016, **117**, 085501.

3 A. J. Mannix, X. F. Zhou, B. Kiraly, J. D. Wood, D. Alducin, B. D. Myers and N. P. Guisinger, *Science,* 2015, **350**, 1513.

4 B. Feng, J. Zhang, Q. Zhong, W. Li, S. Li, H. Li and K. Wu, *Nat. Chem*., 2016, **8**, 563.

5 G. E. Gurr, P. W. Montgomery, C. D. Knutson and B. T. Gorres, *Acta Crystallogr., Sect. B: Struct. Sci*., 1970, **26**, 906.

6 C. T. Prewitt and R. D. Shannon, *Acta Crystallogr., Sect. B: Struct. Sci*., 1968, **24**, 869.

7 T. Edwards, T. Endo, J. H. Walton and S. Sen, *Science*, 2014, **345**, 1027.

8 V. V. Brazhkin, Y. Katayama, K. Trachenko, O. B. Tsiok, A. G. Lyapin, E. Artacho and H. Saitoh, *Phys. Rev. Lett*., 2008, **101**, 035702.

9 K. Trachenko, V. V. Brazhkin, G. Ferlat, M. T. Dove and E. Artacho, *Phys. Rev. B*, 2008, **78**, 172102.

10 A. Vegiri and E. I. Kamitsos, *Phys. Rev. B.*, 2010, **82**, 054114.

11 H. T. Hall and L. A. Compton, *Inorg. Chem*., 1965, **4**, 1213.

12 H. Dong, A. R. Oganov, Q. Wang, S.-N. Wang, Z. Wang, J. Zhang, M. M. Davari Esfahani, X.-F. Zhou, F. Wu and Q. Zhu, *Sci. Rep.*, 2016, **6**, Article No. 31288.

13 A. I. Kharlamov and N. V. Kirillova, *Powder Metall. Met. Ceram.*, 2002, **41**, 97.

14 C. E. Holcombe, Jr. and O. J. Horne, Jr., *J. Am. Ceram. Soc.*, 1972, **55**, 106.

15 A. R. Badzian, *Appl. Phys. Lett.*, 1988, **53**, 2495.

16 D. He, Y. Zhao, L. Daemen, J. Qian, T. D. Shen and T. W. Zerda, *Appl. Phys. Lett*., 2002, **81**, 643.

17 H. Sun, S. H. Jhi, D. Roundy, M. L. Cohen and S. G. Louie, *Phys. Rev. B*, 2001, **64**, 094108.

18 R. H. Wentorf, R. C. DeVries and F. P. Bundy, *Science*, 1980, **208**, 873.

19 A. Y. Liu and M. L. Cohen, *Science*, 1989, **245**, 841.

20 M. Herrmann, I. Sigalas, M. Thiele, M. M. Müller, H.-J. Kleebe and A. Michaelis, *Int. J. Refract. Met. Hard Mater*., 2013, **39**, 53.

21 H. Hubert, B. Devouard, L. A. J. Garvie, M. O'Keeffe, P. R. Buseck, W. T. Petuskey and P. F. McMillan, *Nature*, 1998, **391**, 376.

22 F. P. Bundy, H. T. Hall, H. M. Strong and R. H. Wentorfjun, *Nature*, 1955, **176**, 51.

23 R. H. Wentorf, Jr., *J. Chem. Phys*., 1957, **26**, 956.

24 B. Albert and H. Hillebrecht, *Angew. Chem., Int. Ed.*, 2009, **48**, 8640.

25 H. Bolmgren, T. Lundström and S. Okada, *AIP Conf. Proc.*, 1991, **231**, 197.

26 H. Hubert, L. A. J. Garvie, B. Devouard, P. R. Buseck, W. T. Petuskey and P. F. McMillan, *Chem. Mater.*, 1998, **10**, 1530.

27 R. Naslain, in *Boron and Refractory Borides*, ed. V. I. Matkovich, Springer, Berlin, 1977, p. 139.

28 T. Akashi, T. Itoh, I. Gunjishima, H. Masumoto and T. Goto, *Mater. Trans.*, 2002, **43**, 1719.

29 C. Brodhag and F. Thévenot, *J. Less-Common Met.*, 1986, **117**, 1.

30 C. Ellison-Hayashi, M. Zandi, F. J. Csillag and S. Y. Kuo, *US Patent 5135892*, 1992.

31 M. Kobayashi, I. Higashi, C. Brodhag and F. Thévenot, *J. Mater. Sci.*, 1993, **28**, 2129.

32 T. Lundström and Y. G. Andreev, *Mater. Sci. Eng., A*, 1996, **209**, 16.

33 M. Olofsson and T. Lundström, *J. Alloys Compd.*, 1997, **257**, 91.

34 H. Dong, A. R. Oganov, V. V. Brazhkin, Q. Wang, J. Zhang, M. M. Davari Esfahani and Q. Zhu, *Phys. Rev. B*, 2018, **98**, 174109.

35 P. M. Bills and D. Lewis, *J. Less-Common Met.*, 1976, **45**, 343.

36 D. Nieto-Sanz, P. Loubeyre, W. Crichton and M. Mezouar, *Phys. Rev. B*, 2004, **70**, 214108.

37 V. L. Solozhenko, O. O. Kurakevych, V. Z. Turkevich and D. V. Turkevich, *J. Phys. Chem. B*, 2008, **112**, 6683.

38 Q. An, K. M. Reddy, H. Dong, M.-W. Chen, A. R. Oganov and W. A. Goddard, III, *Nano Lett.*, 2016, **16**, 4236.

39 G. A. Slack and K. E. Morgan, *Solid State Sci.*, 2015, **47**, 43.

40 S. N. Perevislov, P. V. Shcherbak and M. V. Tomkovich, *Refract. Ind. Ceram.*, 2018, **59**, 32 (*Novye Ogneupory*, 2018, no. 1, 33).

41 M. V. Tomkovich, S. N. Perevislov, I. B. Panteleev and A. P. Shevchik, *Refract. Ind. Ceram.*, 2020, **60**, 445 (*Novye Ogneupory*, 2019, no. 9, 31).

42 S. N. Perevislov, A. S. Lysenkov and S. V. Vikhman, *Inorg. Mater.*, 2017, **53**, 376 (*Neorg. Mater.*, 2017, **53**, 369).

43 S. N. Perevislov, P. V. Shcherbak and M. V. Tomkovich, *Refract. Ind. Ceram.*, 2018, **59**, 179 (*Novye Ogneupory*, 2019, no. 4, 96).

44 S. N. Perevislov, *Refract. Ind. Ceram.*, 2019, **60**, 168 (*Novye Ogneupory*, 2019, no. 3, 49).

45 S. N. Perevislov, I. B. Panteleev, A. P. Shevchik and M. V. Tomkovich, *Refract. Ind. Ceram.*, 2018, **58**, 577 (*Novye Ogneupory*, 2017, no. 10, 42).

46 A. S. Lysenkov, K. A. Kim, D. D. Titov, M. G. Frolova, Y. F. Kargin, N. V. Petrakova, A. V. Leonov, S. N. Perevislov, M. V. Tomkovich and I. S. Melnikova, *J. Phys.: Conf. Ser.*, 2018, **1134**, 012036.

47 S. N. Perevislov, A. S. Lysenkov, D. D. Titov, M. V. Tomkovich, K. A. Kim, M. G. Frolova and I. S. Mel'nikova, *Glass Ceram.*, 2019, **75**, 400 (*Steklo Keram.*, 2018, no. 10, 30).

48 D. D. Nesmelov and S. N. Perevislov, *Glass Ceram.*, 2015, **71**, 313 (*Steklo Keram.*, 2014, no. 9, 14).

49 V. Z. Turkevich, D. V. Turkevich and V. L. Solozhenko, *Superhard Materials*, 2016, **38**, 216.

50 V. Z. Turkevich, I. A. Petrusha, D. V. Turkevich, S. N. Dub, N. N. Belyavina, N. Frage and N. Frumina, *Superhard Materials*, 2008, **30**, 16 [*Sverkhtverd. Mater.*, 2008, **30** (1), 23].

51 E. V. Zubova, *Sov. Phys.-Dokl*., 1971, **16**, 317.

52 P. F. McMillan, H. Hubert, A. Chizmeshya, W. T. Petuskey, L. A. J. Garvie and B. Devouard, *J. Solid State Chem.*, 1999, **147**, 281.

53 D. He, M. Akaishi, B. L. Scott and Y. Zhao, *J. Mater. Res.*, 2002, **17**, 284.

54 X. Jiao, H. Jin, F. Liu, Z. Ding, B. Yang, F. Lu, X. Zhao and X. Liu, *J. Solid State Chem.*, 2010, **183**, 1697.

55 G. V. Tsagareishvili, D. S. Tsagareishvili, Ch. M. Tushishvili, I. S. Omiadze, V. N. Naumov and A. B. Tagaev, *AIP Conf. Proc.*, 1990, **231**, 384.

56 S. Yu, Y. Ji, T. Li, M. Han, G. Wang, X. Yuan, Z. Li and P. Chen, *Solid State Commun*., 2000, **115**, 307.

57 S. Yu, G. Wang, S. Yin, Y. Zhang and Z. Liu, *Phys. Lett. A*, 2000, **268**, 442.

58 I. Solodkyi, H. Borodianska, T. Zhao, Y. Sakka, P. Badica and O. Vasylkiv, *J. Ceram. Soc. Jpn*., 2014, **122**, 336.

59 J. Grabis, D. Rašmane, A. Krūmiņa and A. Patmalnieks, *Mater. Sci*., 2012, **18**, 72.

60 T. Lundström, *J. Solid State Chem*., 1997, **133**, 88.

61 T. L. Aselage, D. R. Tallant and D. Emin, *Phys. Rev. B*, 1997, **56**, 3122.

62 X. Jiao, H. Jin, Z. Ding, B. Yang, F. Lu, X. Zhao, X. Liu and L. Peng, *Mater. Res. Bull*., 2011, **46**, 786.

63 E. N. Ogunmuyiwa, O. T. Johnson, I. Sigalas, M. Hermann and A. S. Afolabi, in *Proceedings of the World Congress on Engineering and Computer Science*, San Francisco, 2014.

64 H. F. Rizzo, W. C. Simmons and H. O. Bielstein, *J. Electrochem. Soc.*, 1962, **109**, 1079.

65 J. Kawai, K. Maeda, I. Higashi, M. Takami, Y. Hayasi and M. Uda, *Phys. Rev. B*, 1990, **42**, 5693.

66 I. O. Kayhan and O. T. Inal, *J. Mater. Sci. Lett.*, 1999, **34**, 4105.

67 D. Demirskyi and O. Vasylkiv, *Ceram. Int.*, 2016, **42**, 14282.

68 T. C. Shabalala, D. S. McLachlan, I. Sigalas and M. Herrmann, *Ceram. Int.*, 2008, **34**, 1713.

69 R. Sasai, H. Fukatsu, T. Kojima and H. Itoh, *J. Mater. Sci.*, 2001, **36**, 5339.

70 A. Andrews, M. Herrmann, T. C. Shabalala and I. Sigalas, *J. Eur. Ceram. Soc.*, 2008, **28**, 1613.

71 P. R. Bush, *PhD Thesis*, University of the Witwatersrand, Johannesburg, 2011.

72 S. N. Perevislov, A. S. Lysenkov, D. D. Titov, M. V. Omkovich, D. D. Nesmelov and M. A. Markov, *IOP Conf. Ser.: Mater. Sci. Eng.*, 2019, **525**, 012074.

73 D. D. Nesmelov, O. A. Kozhevnikov, S. S. Ordan'yan and S. N. Perevislov, *Glass Ceram.*, 2017, **74**, 43 (*Steklo Keram.*, 2017, no. 2, 9).

74 M. G. Frolova, A. V. Leonov, Y. F. Kargin, A. S. Lysenkov, D. D. Titov, N. V. Petrakova, S. N. Perevislov, A. A. Konovalov, M. A. Sevost'yanov and I. S. Melnikova, *Inorg. Mater.: Appl. Res.*, 2018, **9**, 675 (*Materialovedenie*, 2017, no. 12, 32).

75 S. N. Perevislov and D. D. Nesmelov, *Glass Ceram.*, 2016, **73**, 249 (*Steklo Keram.*, 2016, no. 7, 15).

76 A. Andrews, *PhD Thesis*, University of the Witwatersrand, Johannesburg, 2008.

77 J. Dai and Z. Tian, *Appl. Phys. Lett.*, 2021, **118**, 041901.

78 D. Demirskyi, I. Solodkyi, Y. Sakka and O. Vasylkiv, *J. Am. Ceram. Soc.*, 2016, **99**, 2769.

79 M. Thiele, M. Herrmann and A. Michaelis, *J. Eur. Ceram. Soc.*, 2013, **33**, 2375.

80 I. Solodkyi, D. Demirskyi, Y. Sakka and O. Vasylkiv, *Ceram. Int.*, 2016, **42**, 3525.

81 T. C. Shabalala, D. S. McLachlan, I. J. Sigalas and M. Herrmann, *Adv. Sci. Technol.*, 2006, **45**, 1745.

82 O. T. Johnson and I. Sigalas, *Optimization of Boride Containing Boron Suboxide ($B_6O$) Materials*, Lambert Academic Publishing, 2012.

83 O. O. Kurakevych and V. L. Solozhenko, *Superhard Materials*, 2011, **33**, 421 [*Sverkhtverd. Mater.*, 2011, **33** (6), 75].

84 C. Chen, D. He, Z. Kou, F. Peng, L. Yao, R. Yu and Y. Bi, *Adv. Mater.*, 2007 **19**, 4288.

85 S. Veprek, R. F. Zhang and A. S. Argon, *Superhard Materials*, 2011, **33**, 409 [*Sverkhtverd. Mater.*, 2011, **33** (6), 60].

86 G. Liu, Z. Kou, X. Yan, L. Lei, F. Peng, Q. Wang and D. He, *Appl. Phys. Lett.*, 2015, **106**, 121901.

87 H. Itoh, *J. Ceram. Soc. Jpn.*, 2004, **112**, 121.

88 V. L. Solozhenko, O. O. Kurakevich, V. Z. Turkevich and D. V. Turkevich, *Superhard Materials*, 2009, **31**, 1 [*Sverkhtverd. Mater*, 2011, **31** (1), 3].

89 M. Thiele, M. Hermann, C. Müller, T. Gestrich and A. Michaelis, *J. Eur. Ceram. Soc.*, 2015, **35**, 47.

90 J. Grabis, D. Rašmane, I. Šteins and M. Lubāne, *Key Eng. Mater.*, 2016, **674**, 54.

91 H. J. Kleebe, S. Lauterbach, T. C. Shabalala, M. Herrmann and I. Sigalas, *J. Am. Ceram. Soc.*, 2008, **91**, 569.

92 M. Herrmann, J. Raethel, A. Bales, K. Sempf, I. Sigalas and M. Hoehn, *J. Eur. Ceram. Soc.*, 2008, **29**, 2611.

93 E. N. Ogunmuyiwa, O. T. Johnson, I. Sigalas and A. S. Afolabi, *Proceedings of the World Congress on Engineering and Computer Science*, San Francisco, 2014, vol. 2, p. 6.

94 M. Thiele, M. Herrmann, J. Räthel, H. J. Kleebe, M. M. Mueller, T. Gestrich and A. Michaelis, *J. Eur. Ceram. Soc.*, 2012, **32**, 1821.

95 M. Herrmann, H. J. Kleebe, J. Raethel, K. Sempf, S. Lauterbach, M. M. Müller and I. Sigalas, *J. Am. Ceram. Soc.*, 2009, **92**, 2368.

96 M. Thiele and M. Herrmann, *12th Conference of the European Ceramic Society*, Stockholm, 2011.

97 E. N. Ogunmuyiwa, O. T. Johnson and I. Sigalas, *Part. Sci. Technol.*, 2019, **37**, 60.

98 O. T. Johnson, E. N. Ogunmuyiwa, I. Sigalas and M. Herrmann, *Proceedings of International Conference on Manufacturing Engineering and Engineering Management Chemical Engineering and Technology, ICMEEM, World Congress of Engineering (WCE)*, London, 2013.

99 A. N. Nikolaev, I. B. Ban'kovskaya and S. N. Perevislov, *Refract. Ind. Ceram.*, 2020, **61**, 428 (*Novye Ogneupory*, 2020, no. 8, 18).

100 M. A. Markov, S. S. Ordan'yan, S. V. Vikhman, S. N. Perevislov, A. V. Krasikov, A. D. Bykova and M. V. Staritsyn, *Refract. Ind. Ceram.*, 2019, **60**, 385 (*Novye Ogneupory*, 2019, no. 8, 34).

101 M. Herrmann, A. K. Swarnakar, M. Thiele, O. Van der Biest and I. Sigalas, *J. Eur. Ceram. Soc.*, 2011, **31**, 2387.

102 R. Machaka, T. E. Derry and I. Sigalas, *Mater. Sci. Eng. A*, 2014, **607**, 521.

103 K. H. Grote and E. K. Antonsson, *Handbook of Mechanical Engineering*, Springer, New York, 2009, vol. 10.

104 G. A. Slack and K. E. Morgan, *J. Phys. Chem. Solids*, 2014, **75**, 1054.

105 S. N. Perevislov, E. S. Motaylo, E. S. Novoselov and D. D. Nesmelov, *IOP Conf. Ser.: Mater. Sci. Eng.*, 2020, **848**, 012066.

106 M. Herrmann, M. Thiele, K. Jaenicke-Roessler, C. S. Freemantle and I. Sigalas, *J. Eur. Ceram. Soc.*, 2011, **31**, 1771.

107 N. Jacobson, S. Farmer, A. Moore and H. Sayir, *J. Am. Ceram. Soc.*, 1999, **82**, 393.

108 I. Solodkyi, S. S. Xie, T. Zhao, H. Borodianska, Y. Sakka and O. Vasylkiv, *J. Ceram. Soc. Jpn.*, 2013, **121**, 950.

109 H. Itoh, I. Maekawa and H. Iwahara, *J. Mater. Sci. Lett.*, 2000, **35**, 693.

*Received: 13th August 2021; Com. 21/6643*